Hindawi
Mobile Information Systems
Volume 2022, Article ID 9658966, 15 pages
https://doi.org/10.1155/2022/9658966

Research Article

Improving QGA-ELM Inversion Model of Rice Leaf Area Index Based on UAV Remote Sensing Image

Juntao Gu,[1,2] **Zhongbin Su**,[2] **Rui Gao**,[2] **Yue Wang**,[2] **Ying Meng**,[2] **and Qingming Kong**[2]

[1]*Agricultural Engineering Post-Doctoral Research Station, Northeast Agricultural University, Harbin 150030, China*
[2]*School of Electronic Engineering and Information, Northeast Agricultural University, Harbin 150030, China*

Correspondence should be addressed to Qingming Kong; kkqqmmmm@126.com

Received 30 October 2021; Revised 8 December 2021; Accepted 4 March 2022; Published 30 March 2022

Academic Editor: Jinan Fiaidhi

The leaf area index (LAI) is an important physiological parameter that characterizes the growth of crops. Traditional measurement could not meet the demands of large-scale accurate monitoring. QGA-ELM and LS-SVM algorithm combined with UAV remote sensing images was used to achieve the goal of building large-scale fast inversion modeling of LAI in this paper. Linear and nonlinear models were constructed for comparing the correlation between six spectral indices and LAI by categorizing the nitrogen level. The LS-SVM model was constructed to replace traditional linear model, the determination coefficient of correction set and prediction set (R^2C and R^2P) were 0.6496 and 0.6814; and the root mean square error of correction set and prediction set (RMSEC and RMSEP) were 0.5702 and 0.6842, respectively. The results showed that the inversion of edge objects in noncrop areas was not so stable. In order to address the problem, an improvement based on the extreme learning machine (ELM) and quantum genetic algorithm (QGA) with probabilistic evolution were used to combine with LS-SVM for overcoming the problem which the hidden layer connection weight and threshold randomly generated and solve the problems of slow regression of nonlinear data and insufficient model generalization ability. Compared with traditional linear and nonlinear regression, the QGA-ELM combined with LS-SVM showed the following: (1) improving the optimization ability greatly and avoid the prematurity of GA (genetic algorithm) effectively. The generalization performance has also been enhanced. (2) R^2P of prediction set was 0.6686, and RMSEP was 0.8952 which could reflect the growth and distribution trend of rice in the regional scale. (3) Adapting different fertilization gradients (deficiency to excess) could provide basis for LAI inversion in different varieties and accumulated temperature zone of rice. The results above showed that QGA-ELM combined with LS-SVM could improve the stability of the model greatly and provide reference significance for rice growth inversion.

1. Introduction

The leaf area index (LAI) is the main variable of crop growth monitoring [1]. Accurate estimation of LAI could provide an important basis for pest, growth monitoring and biomass, and yield estimation [2, 3]. Traditional measurement methods mainly used by manual which has lots of limitations [4]. The vegetation indexes (VI) such as NDVI, RVI, and NDRE which has highly correlation with LAI is gradually used for the inversion research recently [5]. The commonly used LAI inversion methods include linear regression, power function regression, and exponential function regression [6]. However, these models usually could not represent well the nonlinear relationship between VI and LAI. With the rapid development of artificial intelligence (AI), more and more intelligent algorithms were applied to the LAI inversion model in recent years; Zhang et al. [7] used the SVM to invert LAI of summer maize, Yao et al. [8] used random forest (RF) to estimate LAI of forest land by remote sensing, and Wang et al. used the back propagation neural network (BPNN) to estimate LAI of maize at different growth stages [9]. Although the above intelligent algorithms had achieved highly inversion accuracy, but there were still much disputes that could not be ignored for that the RF could not make predictions when the data range exceeds the training set, showing over fitting caused by

specific noises [10]. The selection and optimization of SVM kernel function parameters and parameter penalty terms had a significant impact for the modeling [10]. BP network needed a large number of training samples and has the drawback of lower training speed, easy to fall into local optimization, etc.

To solve the problems mentioned above, LAI during different growth period of rice obtained by unmanned aerial vehicle (UAV) remote sensing was chosen as the research object, the nitrogen level classification was realized by image and spectrum [11], and the inversion model was optimized in this paper. The extreme learning machine (ELM) combined with quantum genetic algorithm (QGA) [12] with probabilistic evolution was used to overcome the problem that connection weights of hidden layers and threshold were randomly generated in the traditional model and solved the problems of slow regression of nonlinear data and insufficient generalization ability of model. The accurate inversion and verification of LAI were completed combined with LS-SVR model, and the inversion accuracy, generalization performance, and stability of the model were improved greatly.

2. Materials and Methods

2.1. Research Design. The research area is located in Dehui Rice planting Park of Fangzheng in Heilongjiang Province (Northeast of China); the covering area was about 9000 mu. There was no stress water, fertilizer, disease, and insect pests in the experimental area that could ensure that the rice experimental area was fully grown naturally. The field in the experimental area was divided neatly. Nitrogen was distributed step by step in the plot, and potassium fertilizer was evenly applied twice at jointing stage and heading stage (a total of 75 kg/ha). The experiment lasted from May to September 2018. The experiment was divided into 48 sample units in the field, and the cultivator Wuyoudao 4 was planted. The ground sampling time was within two days after the flight monitoring. Five nitrogen evaluation criteria were set for nitrogen content in rice: severe deficiency of N0, deficiency of N1, partial deficiency of N2, moderate amount of N3, and excessive amount of N4 to simulate the growth of rice in natural ecology. Nitrogen fertilizer was evenly applied to each plot at 40%, 30%, and 30% at regreening stage, jointing stage, and heading beginning stage, respectively.

2.2. Research Samples. The experimental data were collected from 48 sample sites on June 15, July 7, July 26, and August 16 of 2018, respectively, corresponding to the tillering, jointing, booting, heading, flowering, filling, and fruiting stage of rice. LAI, NDVI, and RVI of rice were collected each time. Specific collection methods were as follows:

A 100 cm × 100 cm quadrat was set in 48 plots, and the number of rice plants in the quadrat was recorded. Then, 3 japonica rice plants were randomly selected from each quadrat, and the total number of leaves, leaf length, and leaf width of each rice plant was recorded to calculate the leaf area of each rice plant. The calculation formula of LAI is as follows [13]:

$$LAI = 0.75 \times \rho \times \frac{\sum_{i=1}^{m}\sum_{j=1}^{n}\left(L_{ij} \times B_{ij}\right)}{m}, \quad (1)$$

where 0.75 is the correction coefficient, ρ is the rice planting density, m is the number of rice plants in the plot, n is the number of leaves per rice plant, L_{ij} is the length of the rice leaf, and B_{ij} is the maximum leaf width in the formula.

30 rice canopy leaves were evenly collected in each quadrats at the same time, and the NDVI and RVI values in the middle of the leaves were obtained using the CGMD active light source equipment made by Nanjing Agricultural University, and the average values were, respectively, used as the effective NDVI and RVI values in an experimental plot.

2.3. Research Tools. The fixed-wing UAV was selected as the remote sensing platform for the research. The wingspan was about 4 meters, the fuselage was about 6 meters, the maximum takeoff weight was 30 kg, and the flight speed was between 70 and 120 km/h. The UAV was equipped with the pylon and automatic navigation system, and POS information was recorded during the flight. The UAV was equipped with high-definition digital camera Sony 5100 and 6-channel multispectral camera Micro-MCA6 Snap to obtain a multispectral image data in RAW format. Table 1 lists the parameters of the Micro-MCA6 Snap camera.

2.4. Data Processing and Analysis

2.4.1. Image Stitching Preprocessing. The image range obtained by UAV remote sensing was limited due to the constraints of data acquisition height ,and lens focal length which makes the UAV could not fully cover the required monitoring regional scale. Requiring the synthesis and joining together of the remote sensing image collected for solving the problem of getting all the information in large regional scale, multiple remote sensing images were fused into one image with panoramic effect image Mosaic is the process of automatically stitching image sequences with certain overlapping areas into a panoramic image with a wide field of view. UAV flight image requires a high coincidence rate between adjacent images. 60% course overlap rate and 30% side overlap rate at least should be achieved in general. The UAV flight experiment meets the requirements of image Mosaic.

The three-channel images of feature bands synthesized in PixelWrenc2 software were firstly converted from RAW data format to TIFF format. Then, the initial image stitching was completed in the Pix4D Mapper. Figure 1 showed the sparse digital surface model in the stitching process. Feature points were extracted and separately spliced using the optimized SIFT algorithm to solve the phenomenon of lost image in the edge part; finally, a complete image was synthesized in the Pix4D Mapper; initial mosaic image and optimizing feature points maps are shown in Figure 2. Geometric correction and radiometric correction are carried out to prevent distortion and at the same time eliminate the

Table 1: Specifications of the Micro-MCA6 Snap camera.

Project	Parameter
Sensor type	CMOS
Sensor size	6.66∗5.32 mm
Number of lenses	6
Effective pixels	1.3 million
Image resolution	1280∗1024
Image format	RAW, DCM
Channel center wavelength	490 nm, 550 nm, 680 nm, 720 nm, 800 nm, 900 nm
Camera weight	0.7 kg
Memory card	16 GB SD memory card per channel (6 in total)
Other	Remote shutter and external GPS module

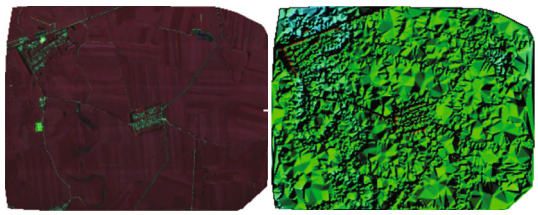

Figure 1: Orthomosaic and the corresponding sparse digital surface model (DSM) before densification.

characteristic distortion caused by atmospheric transmission, sensor itself, terrain, and other systematic and nonsystematic reasons. The geometric correction error of the image was confirmed to be less than 0.5 pixels [14] based on 30 ground control points and map coordinates near the test area.

2.4.2. Digital Image Preprocessing. RGB image was a color space model represented by three-dimensional coordinate system, but the representation of image details was not so complete; HSV color space transformation was carried out on the image for solving the problem mentioned above which could achieve more accurate effect in the classification of ground object model. The formula for HSV color space conversion from RGB color space was as follows:

$$H = \begin{cases} 60\dfrac{G-B}{\max-\min}, R = \max \\ 60\dfrac{2+(B-R)}{\max-\min}, G = \max \\ 6\dfrac{4+(R-G)}{\max-\min}, B = \max \\ H = 360, H < 0 \end{cases}, \quad (2)$$

$$V = \max/255,$$

$$S = \frac{\max-\min}{\max}.$$

HSV color space is an inverted cone model; the color space model is shown in Figure 3.

H represents different colors, ranging from 0 to 360. Among them, 0 and 360 represent blue, 120 represents green, and 240 represents red. S represents different shades of color, ranging from 0.0 to 1.0. The higher the value is H, the purer the color is S. V indicates the change in brightness. The value ranges from 0 to 1. The higher the value, the brighter the color. The RGB image of the core area of the park in August 2018 was taken as an example to complete HSV color conversion.

3. Results and Discussion

3.1. Analysis of Rice Nitrogen Levels Based on Supervised Classification

3.1.1. Support Vector Supervised Classification. Traditional inversion models usually did not decompose the nitrogen level in the test area. A large amount of near-earth data was usually used for comparison. The representativeness and universality of the model could not be used to determine the regional differences. The classification of nitrogen level based on image and spectrum was carried out for specific test areas in the research. The experimental fields with different fertilization treatments, different growth conditions, and different nutritional compositions were classified from the image perspective; the representativeness of the model was clarified; and the later model improvement was provided with judgment basis and data support. The growth of crops which were treated with different fertilization can effectively determine growth state, and the classification of nitrogen levels could effectively reflect LAI distribution characteristics and features [15]. For getting the preliminary understanding of the growth of rice in the study area, ten fields of research areas were taken as examples to classify rice canopy nitrogen in ENVI, and the RGB images, multispectral images, and HSV images were classified, respectively. Exploring the classification effect of different images and algorithms in nitrogen classification, the supervised classification (training classification method) used in this paper and the process of remote sensing images are shown in Figure 4.

SVM is a machine learning method based on statistical learning theory [16]. It could spontaneously find a support vector with greater distinguishing ability for each

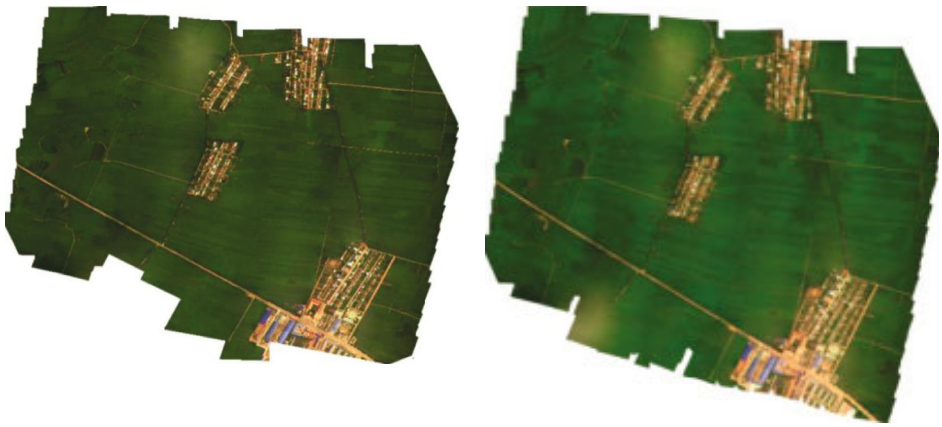

(a) PIX4D Mapper initial mosaic image (b) PIX4D Mapper after optimizing feature points

Figure 2: PIX4D Mapper splicing image.

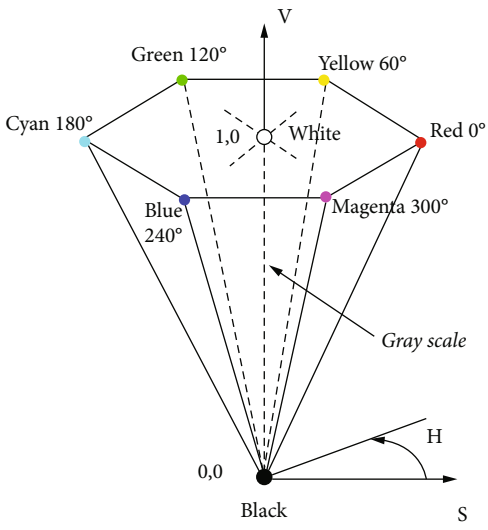

Figure 3: HSV color space model.

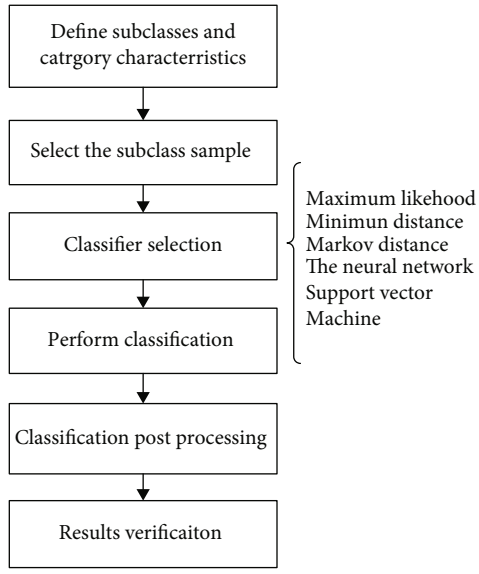

Figure 4: Supervised classification flow chart.

subcategory and constructed a classifier from this, thereby maximizing the interval between each subcategory, so it has a higher classification accuracy. SVM was used to classify nitrogen levels in this paper, and the samples for supervised classification were defined by using the ROI tool which was from the ENVI software. The classification category was determined with different features; regardless of crop growth state, supervised samples selection results are shown in Figure 5.

RGB images, multispectral image, HSV color space image, and NDVI images were classified and used to explore the features which is most suitable for classification. Multispectral was selected and gaved up hyperspectral was mainly due to the NDVI was composed by the fixed band of red and near-red band. The hyperspectral camera has the features of comprehensive and continuous spectral; the wavelength range covers from 400 to 1000 nm which is suitable for the searching and selecting of characteristic bands. However, due to the requirements of overweight and high stability, the acquisition process and data transmission are not easy to achieve. In contrast, the multispectral camera has 6 channels and 12 bands, which can complete red, near red, and other bands, making it more suitable for agricultural production monitoring parameters such as leaf area index or biomass. The classified images of ground features by SVM are shown in Figure 6.

3.1.2. Classification of Accuracy Evaluation. Using classification statistical tools in ENVI software to construct a confusion matrix for the evaluation of nitrogen level classification accuracy is shown in Table 2. The selection of samples in the training area was the most important factor that affects the classification results in SVM supervised classification. In the classification process, there was less manual intervention, so the error caused by human factors could be ignored that could be seen from the classification results that the RGB image has poor classification ability for N0 and N2 subcategories, which may be related to the growth of rice in the area to be classified. The mapping accuracy of the N3

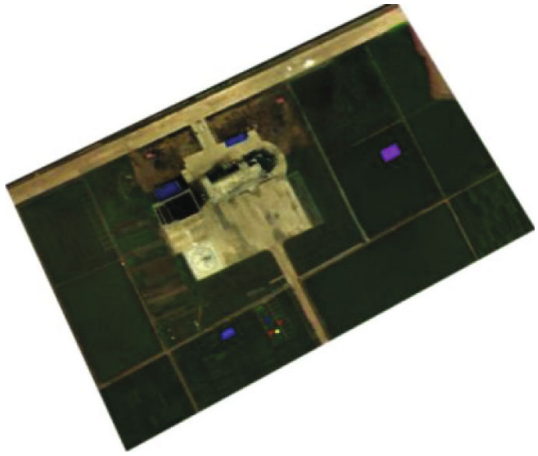

(a) RGB image nitrogen level classification image

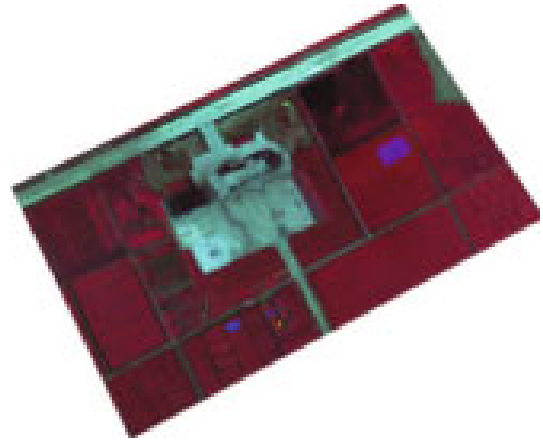

(b) Multispectral classification of nitrogen levels classification image

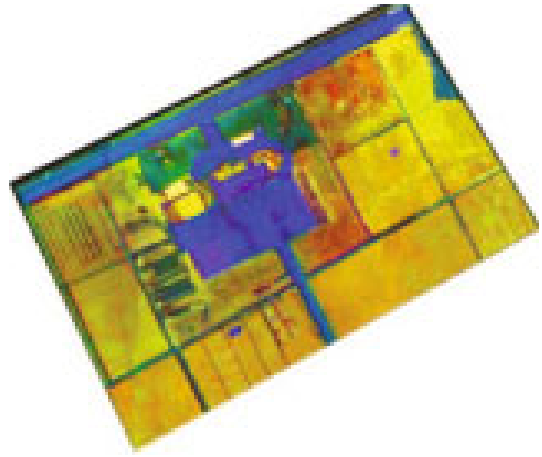

(c) HSV image nitrogen level classification image

Figure 5: Nitrogen level classification image.

and N4 subcategories could reach more than 95%; HSV images are similar to RGB images, and the classification ability of low-nitrogen subcategories was poor. The classification effect of the high nitrogen subcategory was better; MS images also achieve a better classification effect, and the classification of the N2 subcategory has obvious advantages. Horizontal comparison of all classifications of N0-N4 subcategories shows that the overall recognition of N0, N1, and N2 subcategories was not so well which means that it was difficult to accurately distinguish the state of nitrogen deficiency at the level of low-altitude remote sensing images.

3.2. Construction of LAI Inversion Model

3.2.1. LS-SVM Linear Model Construction. LS-SVR includes least squares and support vector machine which is mainly based on the machine learning method in statistical learning theory. The biggest difference between LS-SVR and SVM is that replacing the loss function of the original method, which greatly facilitates the solution process of lagrange multiplier. LS-SVR algorithm has fewer parameters to be selected compared with other algorithms and the parameters that could significantly affect the accuracy of the model only include kernel function type, penalty coefficient C, and kernel function parameter g which has better stability and faster operation speed. At the same time, LS-SVR could also reduce the computational complexity through support vector and has the ability of the kernel to fit samples at high latitude; during the calculation, extracting factors could solve the long time-consuming and complex data fitting problem which reduced the data dimension.

The correlation between vegetation characteristic spectral band [17]and rice leaf LAI was analyzed firstly. A variety of broad-band indices such as normalized vegetation index (NDVI) and ratio vegetation index (RVI) are selected for the LAI estimation model in this article. The spectral index is shown in Table 3.

The method of comparing the correlation between VI and LAI was the same as that of the chlorophyll method. Using the sample area of the training set collected on the

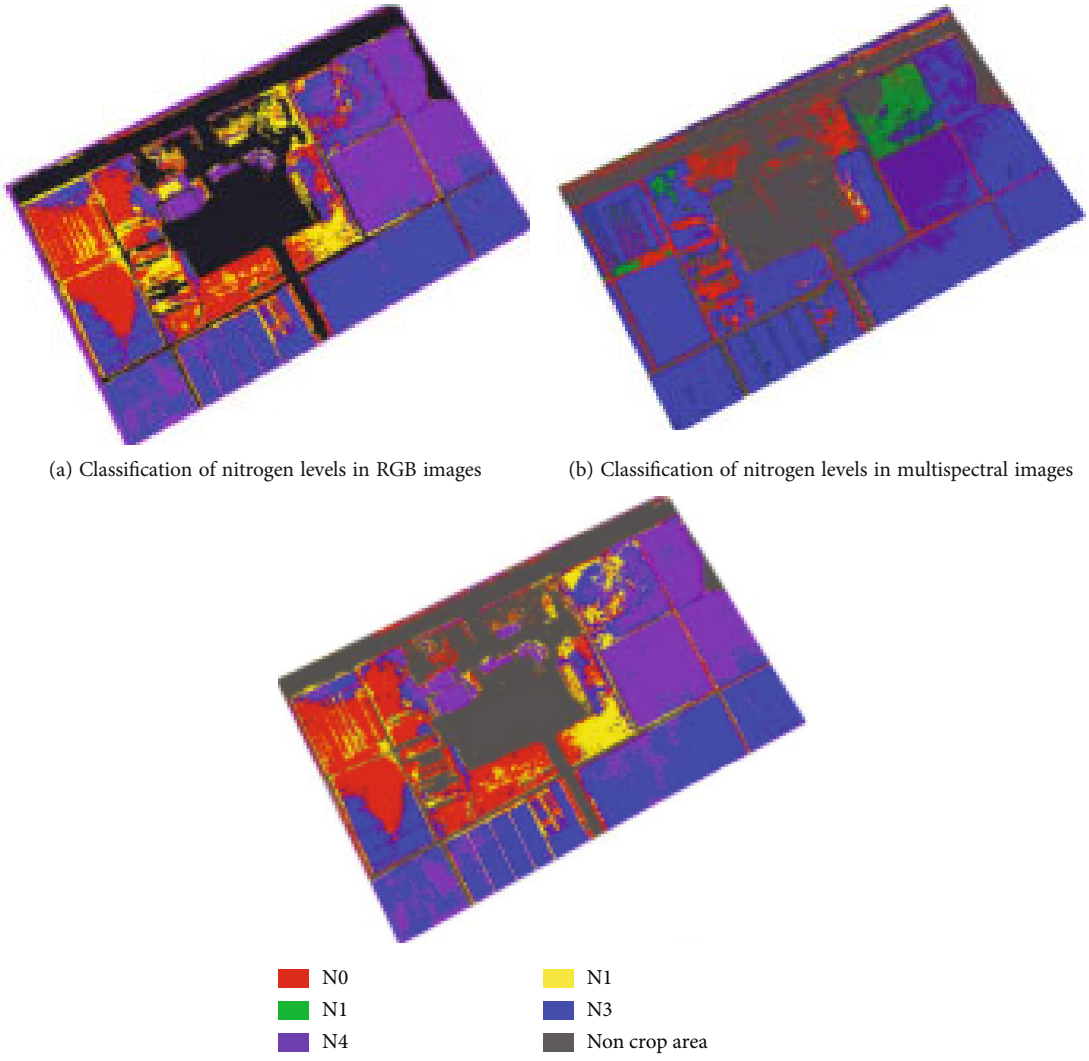

(a) Classification of nitrogen levels in RGB images

(b) Classification of nitrogen levels in multispectral images

(c) HSV image classification of nitrogen levels

Figure 6: Nitrogen classification based on SVM.

Table 2: Confusion matrix of SVM classification.

Type	RGB image				HSV image				Multispectral image			
	C [a]	O [b]	P [c]	U [d]	C [a]	O [b]	P [c]	U [d]	C [a]	O [b]	P [c]	U [d]
N0	50.54	11.54	88.46	49.46	100.0	100.0	0.00	0.00	47.46	10.58	89.42	52.54
N1	36.36	53.33	96.58	95.76	66.67	91.67	8.33	33.33	40.82	51.67	48.33	59.18
N2	0.00	100.0	0.00	0.00	100.0	100.0	0.00	0.00	66.67	98.53	1.47	33.33
N3	4.24	3.42	96.58	95.76	67.72	64.96	35.04	32.28	5.54	5.34	94.66	94.46
N4	1.37	1.64	98.36	98.63	0.00	0.27	99.73	100.0	2.01	1.92	98.08	97.99
Noncrop	0.56	0.00	100.0	99.44	100.0	100.0	0.00	0.00	0.56	0.00	100.0	99.44
Total	Total accuracy (%) = 92.60				Total accuracy (%) = 63.91				Total accuracy (%) = 92.14			
	Total accuracy (%) = 0.8811				Total accuracy (%) = 0.4152				Kappa coefficient = 0.8736			

ground, the independent variable x was set to each VI, and the dependent variable y was set to LAI, and the fitting model was established based on the empirical model analysis method. The model determination coefficients R^2 and RMSE were used as the correlation evaluation criteria to evaluate the fitting results of the six indices in Table 4, and then the best VI for retrieving the LAI of japonica rice was obtained.

The VI used for LAI inversion in the table all reached the significant level of $P = 0.05$, when the coefficient of determination R^2 of the empirical model was higher and the RMSE

Table 3: Spectral index for rice LAI inversion.

Object	Formula	Provenance
Ratio vegetation index (RVI)	ρ_{NIR}/ρ_R	Pearson et al. (1972)
Normalized vegetation index (NDVI)	$(\rho_{NIR} - \rho_R)/(\rho_{NIR} + \rho_R)$	Rouse et al. (1974)
Green normalized vegetation index (GNDVI)	$(\rho_{NIR} - \rho_G)/(\rho_{NIR} + \rho_G)$	Gitelson et al. (1996)
Optimizing soil regulation vegetation index (NPCI)	$(\rho_R - \rho_B)/(\rho_R + \rho_B)$	Schleicher et al. (1994)
Nitrogen balance index (NRI)	$(\rho_{-}\rho_R)/(\rho_R + \rho_G)$	Penuelas J, et al. (2001)
Approximate red edge position index (s-REP)	$[(\rho_{710} + \rho_{800})/2 - \rho_{710}]/(\rho_{730} - \rho_{710})$	This article

Note: ρ_{NIR},ρ_R,ρ_G, and ρ_B represent the reflectivity of the rice canopy near infrared, red, green, and blue bands, respectively.

Table 4: LAI inversion models and their spectral index evaluation indicators.

Vegetation index	Model	R^2	RMSE
RVI	$y = 0.1798x + 2.917$	0.6373	0.7759
NDVI	$y = 8.5154x - 1.8625$	0.6912	0.6405
GNDVI	$y = -9.278x + 0.9815$	0.4539	0.9521
NPCI	$y = 10.09x - 3.482$	0.4978	0.9131
NRI	$y = 11.17x + 0.971$	0.5616	0.8531
s-REP	$y = -0.0186x + 8.315$	0.5282	0.885

Table 5: LAI inversion models and their spectral index evaluation indicators.

Vegetation index	Model	R^2	RMSE
RVI	$y = 0.5323x + 2.561$	0.5002	0.6248
NDVI	$y = 0.6945x + 0.9751$	0.5485	0.7399
GNDVI	$y = 0.8x + 1.456$	0.3530	1.2720
NPCI	$y = 0.4653x + 2.873$	0.3036	0.9798
NRI	$y = 0.8164x + 1.394$	0.4298	0.8867
s-REP	$y = 0.5023x + 2.344$	0.4191	0.8949

was smaller. Among the 6 cropping indices, NDVI, RVI, NRI, and s_REP have better inversion effects on rice LAI, with a determination coefficient R^2 above 0.52, and a root mean square error between 0.64 and 0.90. The two VIs, GNDVI and NPCI, are not very effective in the inversion of LAI from heading to filling stage of japonica rice. The coefficient of determination R^2 was below 0.5, and the root mean square error was between 0.9 and 1.0. Among them, the NDVI has the best inversion effect. The model determination coefficient R^2 was 0.6912, and the root mean square error RMSE was 0.6405, which is the best among the 6 VIs, so the NDVI was selected for the inversion of field japonica rice LAI in this paper.

The predictive ability of samples was tested in the unknown verification area in order to test the prediction accuracy of each index model. The verification set sample area (20) were used as the object, and the VI models are used to predict the verification set samples. Set the independent variable x as the actual measured canopy LAI of japonica rice and the dependent variable y as the LAI value in the same area obtained from the inversion of each VI model for fitting regression, with the model determination coefficient R^2 and the root mean square error RMSE as the main indicators, and combine the slope and offset of the fitting equation to evaluate the accuracy of the prediction model. The inversion models results are shown in Table 5.

The prediction results of each VI for the unknown sample subset are quite different. The determination coefficient R^2 of the NDVI and RVI index models was more than 0.5, the RMSE of the RVI index reached 0.6248, the slope of the NRI index was 0.8164 in the prediction models, and the offset was 1.394 at least. Table 5 showed that the index models built underestimate the LAI value from heading to grain filling period in this paper. A comprehensive comparison of the various indexes shows that the model determination coefficient R^2 of the NDVI index was 0.5485, the root mean square error RMSE was 0.7399, the slope was 0.6945, and the offset was 0.9751. Therefore, the prediction effect of the inversion model based on the NDVI index was better. Comprehensively compare the fitting results of the VI on the training set and the validation set, and select the NDVI as the optimal index for retrieving the rice canopy LAI.

3.2.2. Evaluation of the Estimation Ability of Each Model for Different Levels of LAI. For studying the predictive ability of each index model for LAI values in different intervals, all sampled LAI values are divided into three subsets: LAI < 4.4, low interval LAI sample subset; $4.4 \leq$ LAI < 5.5, medium interval LAI sample subset; and LAI ≥ 5.5, a subset of LAI samples in the high interval. Each index model is used to predict the LAI of each sample interval in turn, and the actual measured value and the predicted value are fitted, and the RMSE of the fitting result is used as the evaluation basis, when the RMSE of each subset is in good agreement which indicates that the VI had a better ability to predict LAI in different intervals from Figure 7.

With the increase of the LAI value, the estimation of the LAI by the VI showed saturation to varying degrees. RMSE values of prediction results are shown in Figure 7; NRI index has the best consistency among the six indexes which means that the NRI index performs better in LAI estimations in different intervals. The S_REP index has good estimation ability for LAI samples in the mid-range, but its range was the largest among the 6 VIs, which was 0.1751. The estimation

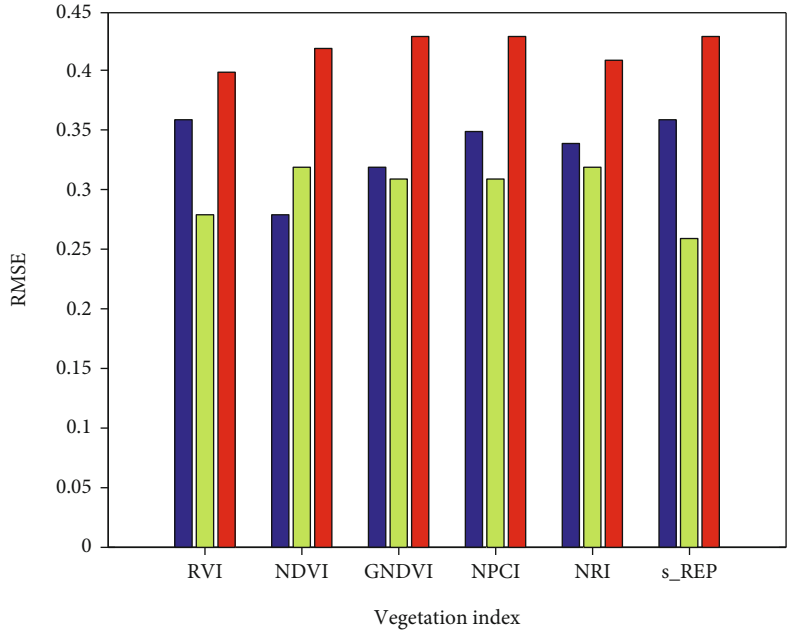

Figure 7: RMSE values of prediction results for sample subsets with different LAI concentrations.

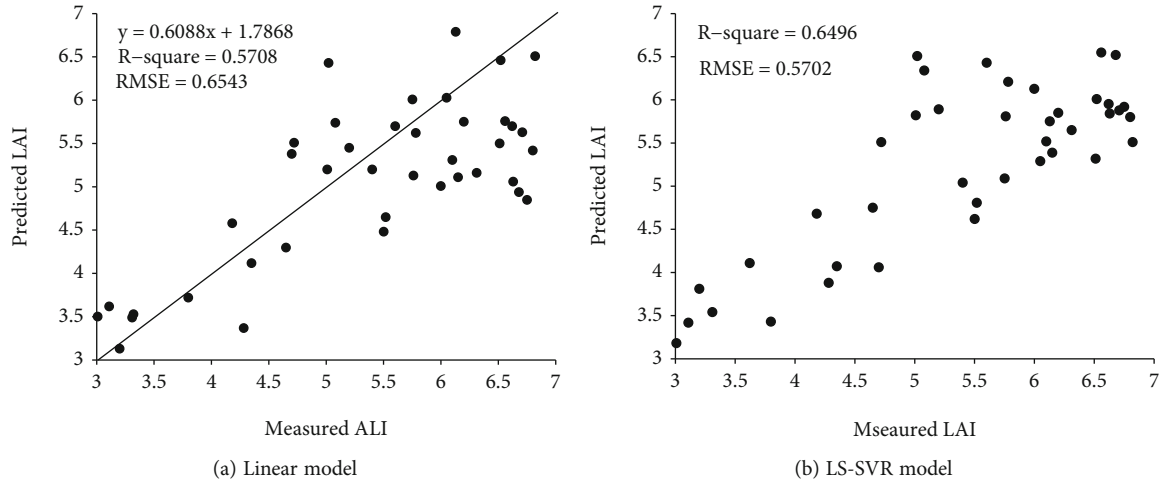

(a) Linear model (b) LS-SVR model

Figure 8: Measured value versus fitted value of linear and LS-SVR models in calibration set of LAI.

ability was affected by the sample interval; NDVI predicts the middle and low LAI sample intervals.

The independent variable x was selected NDVI index as the previous research method, and the dependent variable y was the measured LAI value of field japonica rice. 40 samples of the training set are used to establish the LAI inversion LS_SVR model as shown in Figure 8.

Note: y is the estimated value, X is the ground measured value, R^2 represents the determination coefficient of the fitting model of the training set, and RMSE is the corresponding root mean square error.

Radial basis kernel function and grid search method to obtain the global optimal solution of the penalty coefficient c and the RBF parameter g were used in this model; among them, $c = 7.5$, and $g = 0.65$. Fit the measured values of the training set samples with the estimated values of the NDVI empirical model and the LS_SVR model, and the results are shown in Figure 9. The measured and predicted values of the two models on the training set reached a significant level of $P = 0.05$. Compared with the empirical model, the slope of the equation of the LS_SVR model was closer to 1, and the offset was smaller, indicating that the predicted LAI value was closer to the true value. The LS_SVR model has a more obvious optimization effect on the sample interval below LAI< 5. The NDVI linear model and the LS_SVR model were fitted to the measured and predicted values of 30 samples of the verification machine to test the prediction effects of the two models on the unknown samples. The fitting effect is shown in Figure 10. The closer the measured value and the estimated value are to the diagonal line of $y = x$, the more accurate the estimation accuracy was. Both models underestimate the measured values of validation sets

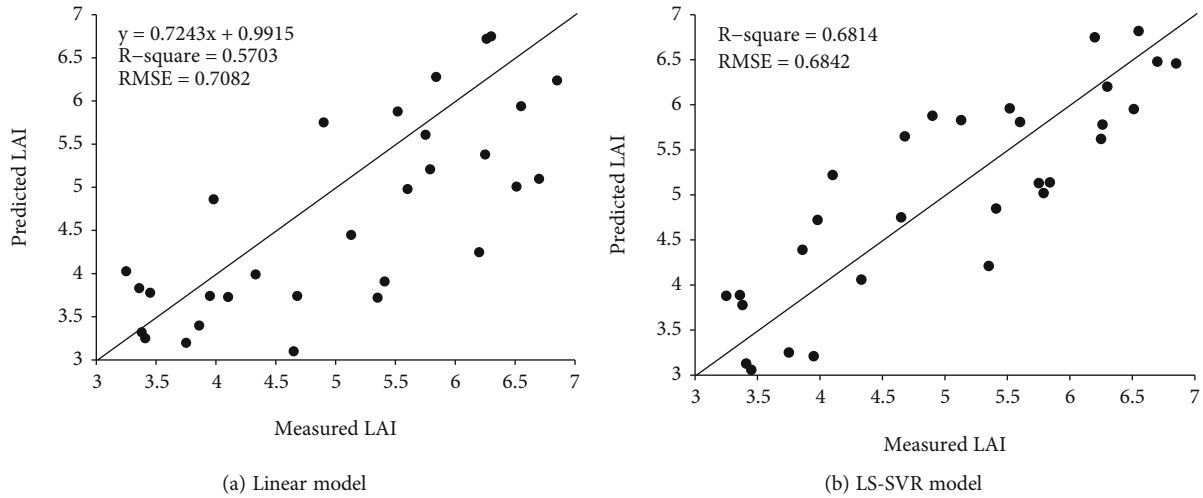

(a) Linear model (b) LS-SVR model

Figure 9: Measured value versus predicted value of the linear and LS-SVR models in prediction set of LAI.

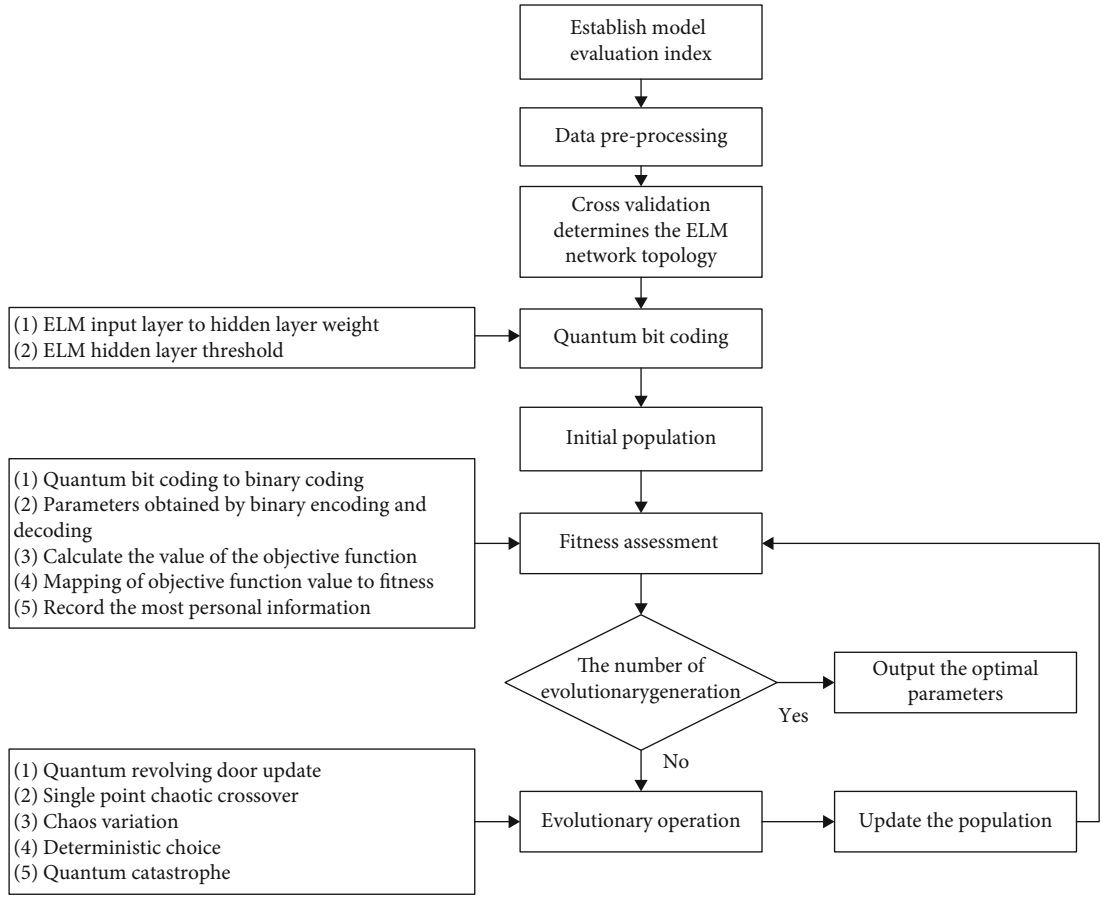

Figure 10: Flowchart of improved QGA-ELM algorithm.

from the perspective of slope; the LS-SVR model performs better than linear that could be also seen form the offset (both less than 1); the LS-SVR showed better prediction ability. The prediction of this model was good; from the determination coefficient and root mean square error of the fitting result, the R^2 of the LS_SVR model of the NDVI index is closer to 1, and the RMSE is smaller than that of the empirical model. Therefore, the LS_SVR model performs LAI inversion results.

3.2.3. Improved Nonlinear Model Construction Based on ELM-QGA. In view of the problem that traditional quantum

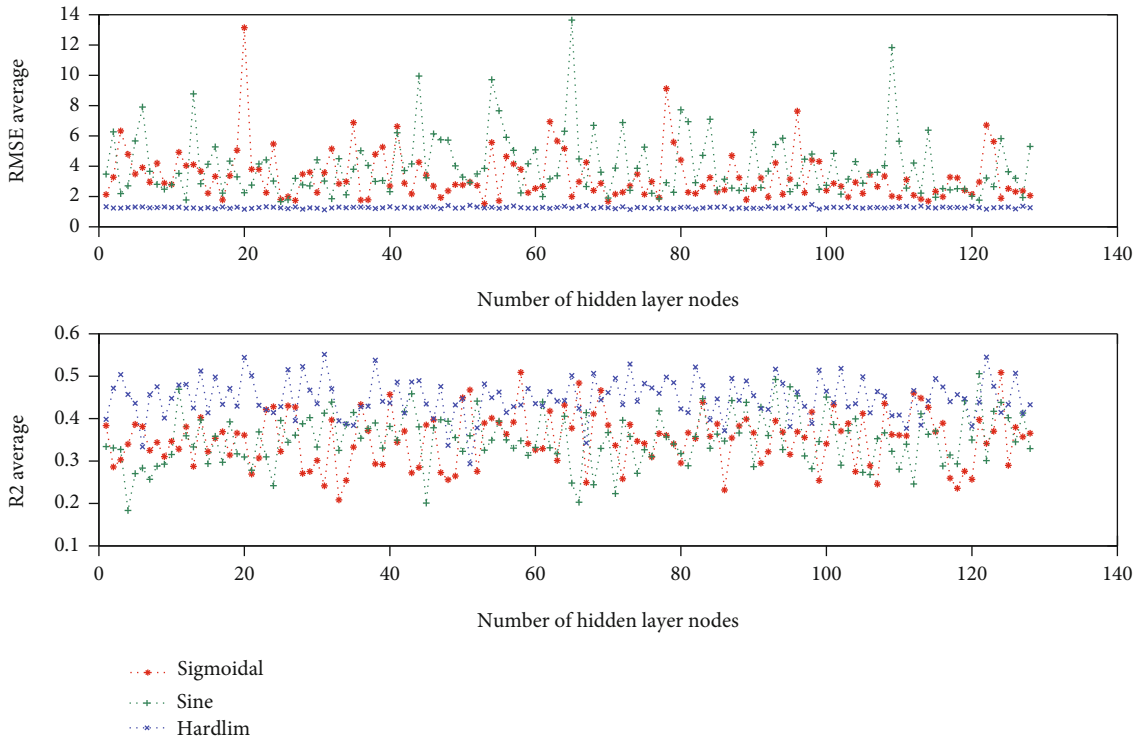

Figure 11: Number of hidden layer nodes with mean values of RMSE and R^2.

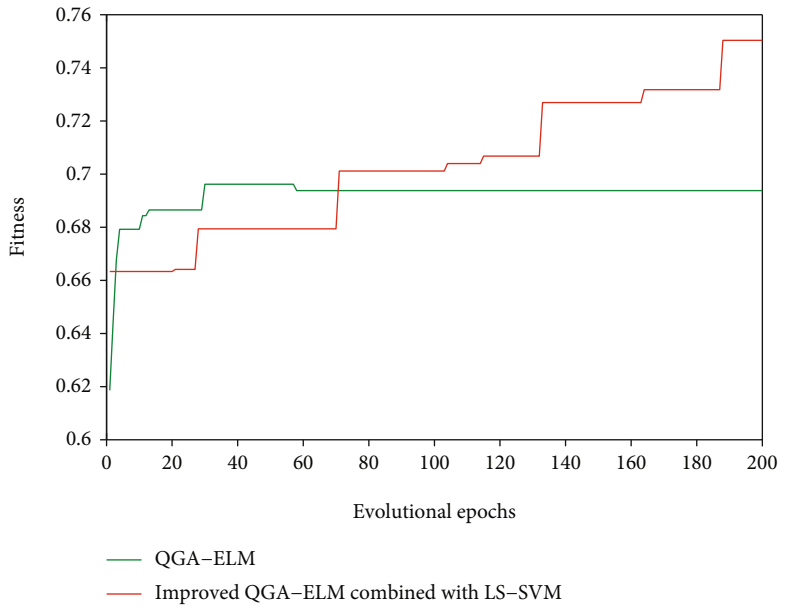

Figure 12: Comparison of evolutionary processes.

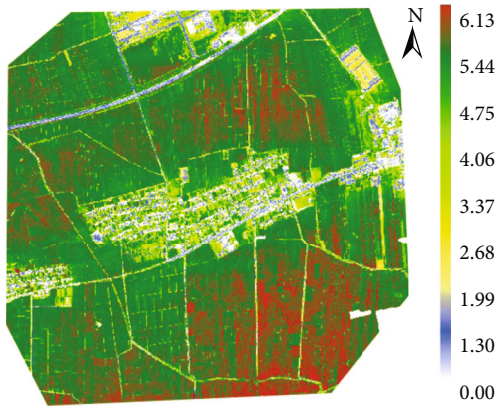

Figure 13: Spatial distribution map of race LAI in DeSheng.

genetic algorithm uses fixed rotation angle to search result that was unstable, in order to speed up the algorithm execution speed, the search table was abandoned in this study, and the rotation angle size and rotation angle direction are determined directly by comparing the current binary solution with the optimal binary solution. Define the binary angle as follows:

$$\theta i = \begin{cases} 0 \cdots\cdots\cdots x_i = 0 \\ 0.01\pi \cdots x_i = 1 \end{cases} \quad (3)$$

In this definition, x_i represents the i bit of the binary solution x and θ_i represents the angle corresponding to the binary bit. The rotation angle of this article is defined as follows:

$$\Delta\theta_i = k(\theta_{Besti} - \theta_i) \quad (4)$$

In this definition, θ_{Besti} represents optimal binary solution and θ_i represents the angle corresponding to the i bit in the current solution. k was the adjustment coefficient, which is defined as follows:

$$k = \left(1 - \frac{n}{N}\right) \times \frac{f(best)}{f(x)} \quad (5)$$

In the formula, N is the maximum evolutionary algebra, n is the current evolutionary algebra, and f(best) is the optimal solution adaptation value which represents the current solution adaptation value $f(best), f(x), n, N > 0$.

At the same time, because biological evolution was randomness plus feedback, adding chaos operation to the evolutionary algorithm can effectively improve the algorithm's search for excellence. Using the sequence $x(n+1) = 4x(n)(1 - x(n), n = 0, 1, 2 \cdots N - 1)$ to produce a chaos value for each generation, firstly, $x(0)$ was a random number at (0,1), and then the crossing position of each generation was determined according to the chaotic sequence. After sorting according to fitness, two adjacent individuals are crossed to form a single point chaotic crossing. Finally, setting the mutation rate and random threshold, the mutation number of each generation was determined by the chaotic sequence and random threshold. The number of mutations was determined by the mutation rate. The mutation position generated randomly, and the corresponding quantum bit is flipped to complete the mutation operation, thus forming chaotic mutation, and introduces a deterministic selection strategy to combine the original population Q, the population after the rotation of the quantum revolving door called Q_1, the population after a single point chaotic crossover population called Q_2, and then the population after the chaotic variation called Q_3.Then merge them together. The k individuals were selected from the merging, with the highest fitness that was selected as the new population Q' to participate in the next generation evolution, where k was the size of the original population [18].

Finally, quantum catastrophe operation was added and when the optimal solution of the population continues to evolve for 5 generations remains unchanged; the k/2 individuals with the least fitness in the population are randomly reconstructed, where k was the size of the original population, so as to exert a large disturbance effect on the population and increase the possibility of finding the global optimal solution. The improved QGA-ELM algorithm flow is shown in Figure 10.

(1) Cross-Validation Determines the ELM Network Topology. Nearly 70% data was randomly selected from 208 sets of data as the training set, and the remaining 30% data was used as the test set in this paper, thus obtaining 144 sets of training set data and 64 sets of test set data. Select the input of the NDVI and RVI corresponding models and the output of LAI corresponding models. In order to reduce the effect of variable difference on model performance, all the data are normalized before simulation, and the corresponding reverse normalization operation was carried out after simulation. In this paper, the 8 fold cross-validation method was selected, where the number of hidden layer nodes is set to 1 to 128 and the implicit layer activation functions are set to "Sigmoidal," "Sine," and "Hardlim." Figure 11 shows the number of hidden layer nodes along with the mean of RMSE and the number of hidden layer nodes along with the mean of R^2.

The comparison of evolutionary processes is shown in Figure 12; the mean of RMSE and R^2 from the network structure which the hidden layer function uses the "Hardlim" is better than the function using "Sigmoidal" and "Sine," so this paper chooses "Hardlim" as the hidden layer function. Secondly, when the hidden layer function is "Hardlim," the RMSE value fluctuates very little with the number change of hidden layer nodes, which can be even ignored. So the best hidden layer function of ELM network is "Hardlim" and the best number. Under the circumstances of this, the average values of RMSE and R^2 are 0.5642 and 1.11023, respectively.

(2) Comparison between QGA-ELM Algorithm and Improved QGA-ELM Algorithm. The improved and not improved QGA-ELM algorithms are performed 10 times each, And the evolutionary process with the highest evolutionary

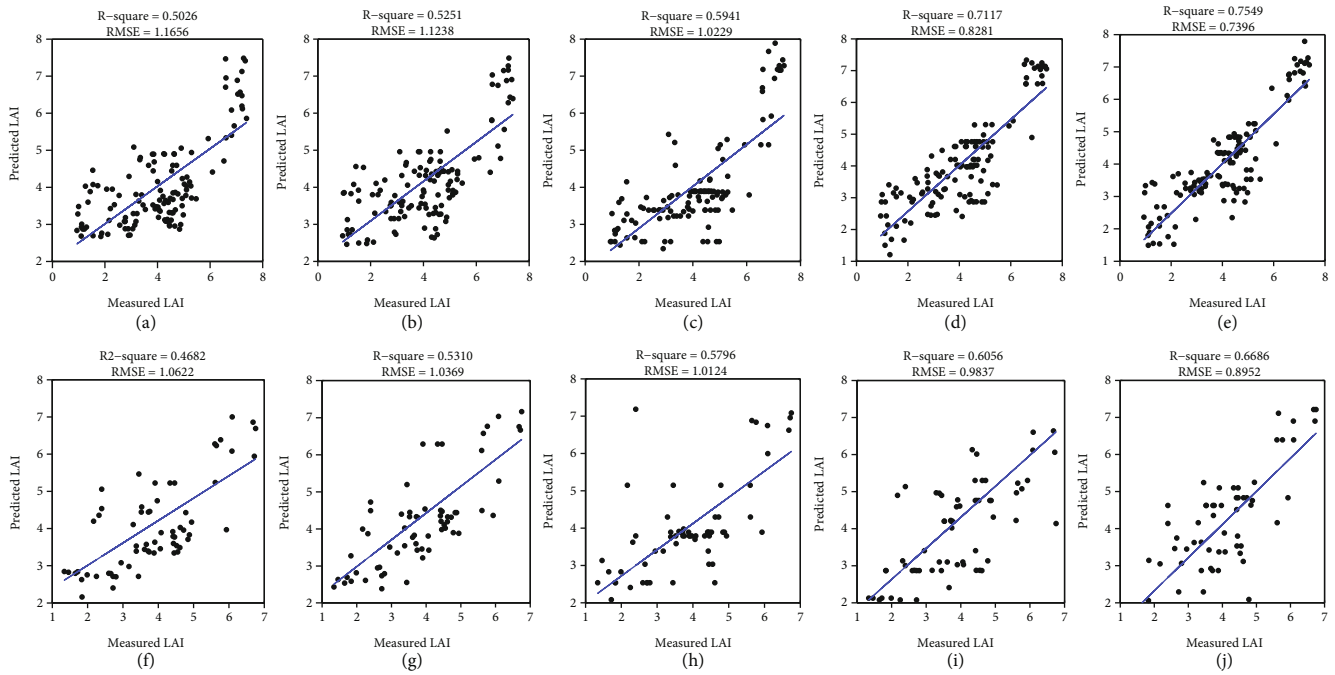

Figure 14: Comparison of inversion results of training set.

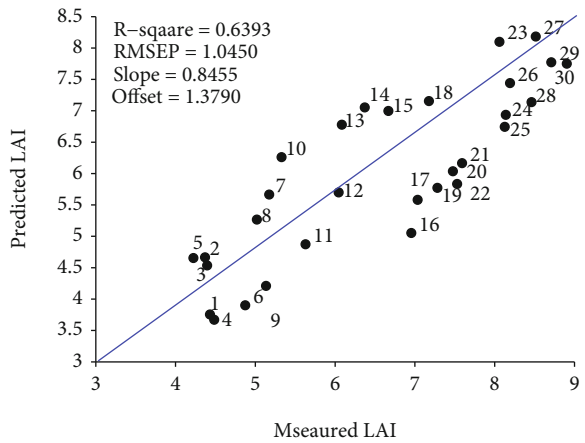

Figure 15: Measured values of LAI versus inversion values.

fitness of both is drawn in Figure 3, where the adaptability is the mean of R^2 under the circumstances of 8 fold cross-validation.

From the evolution line given in Figure 13, QGA-ELM algorithm founded the optimal adaptability to be 0.6962, while the modified QGA-ELM algorithm in out work finds the optimal fitness to be 0.7503. The effect has increased by 7.77%, and the frequency of adaptation changes in the evolution process is more than that of the unimproved algorithm, which shows that the improved algorithm based on this work can effectively improve the model's optimization ability, avoid premature of the algorithm, and reduce the risk of falling into local optima which meets the conclusion of references. Optimal probability and better results can be found so that the modified algorithm possesses a high practical value.

(3) The Comparison of Inversion Effect on Datasets. In order to test the universality and effectiveness of the modified QGA-ELM model, establish five models of MLR, BP, ELM, QGA-ELM, and QGA-ELM with LS-SVM in sequence, and compare inversion effects on different datasets. BP adopts a single hidden layer structure. The number of hidden layer nodes is determined by an empirical formula and then determined as 3 through cross-validation. The transfer functions of the input layer to the hidden layer and the hidden layer to the output layer are, respectively, "tansig" and "purelin". The largest time of iterations was 2500, and the error was set to 0.0001.

The inversion effect diagrams of the five models on the training set and the test set are shown in Figure 14. The explanations are as follows: (1) The improved QGA-ELM algorithm had the highest inversion accuracy and the lowest error both in the training set and the test set among the five models. (2) The inversion accuracy of the ELM inversion model optimized by the QGA had been greatly improved, and the QGA-ELM combined with LS-SVM algorithm had improved the inversion accuracy compared to the unmodified algorithm. (3) The inversion accuracy of the BP model and the three ELM models on the training set and test set was higher than that of multiple linear regression model, indicating that there was a strong and nonlinear relationship rather than linear relationship between VI and LAI. (4) The R^2 of training set in QGA-ELM combined with LS-SVM inversion model is 0.7549 RMSE is 0.7396, and the R^2 of the prediction set is

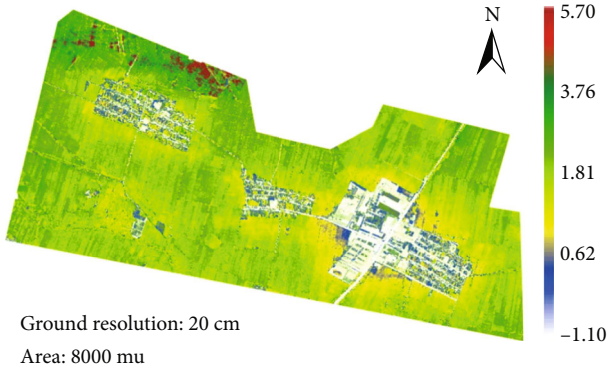

(a) Spatial distribution map of race LAI in Hongxing

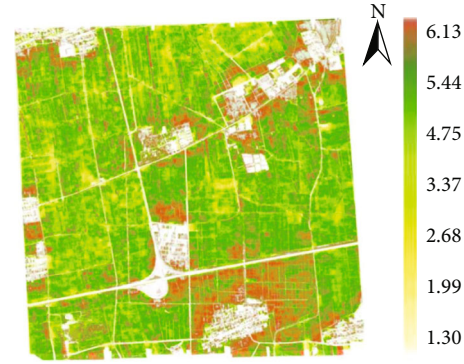

(b) Spatial distribution map of race LAI in Anle

(c) Spatial distribution map of race LAI in Linmin

Figure 16: Spatial distribution map in three farms.

Table 6: Biomass and yield inversion models based LAI of rice.

Index	Rice growth period	Model	R^2P	RMSEP
Biomass (kg/m^2)	Heading stage	$y = 0.2608x + 0.0742$	0.8583	0.332 kg/m^2
	Prophase of booting	$y = 0.5602x - 0.1227$	0.8188	0.406 kg/m^2
Yield (kg/mu)	Heading stage	$y = 68.93x + 132.84$	0.8056	30.561 kg/mu
	Prophase of booting	$y = 64.561x + 187.11$	0.8254	37.446 kg/mu

0.6686, RMSE is 0.8952, indicating that the modified inversion model has higher inversion accuracy, lower error and stronger normalization ability.

3.3. LAI Remote Sensing Mapping and Inversion Test. The NDVI index was the optimal index for heading-filling period from the results above, and the LS_SVR model based on the NDVI index had better inversion accuracy. The LAI grading map of Desheng farm was made in ArcGIS. The spatial distribution map is shown in Figure 13 comparing with rice chlorophyll classification maps LAI and chlorophyll are highly consistent, and the growth of rice and the nutritional status are unified to some extent.

For verifying the accuracy of remote sensing mapping, the extra 30 additional samples LAI measured on the ground were fitted with the inversion value of the same area location. The measured and inversion results are shown in Figure 15. The fitting accuracy of the two was higher to some extent. The R^2 of the inversion model is 0.6393, the RMSE is 1.0450, the slope is 0.8455, and the offset is 1.3790. The results show that it was feasible to analyze the growth of field rice based on UAV low-altitude remote sensing images.

In order to verify whether the inversion model is also suitable for rice LAI analysis in unknown areas, the inversion model was used in the drone remote sensing images of Anle, Limin, and Hongxing farms obtained in this experiment; the LAI value grading map is shown in Figure 16. The LAI value of rice in the Red Star Rice Planting Park is obviously underestimated. Among them, the LAI value of a large

area near residential areas is between 1.0 and 2.0, which is caused by the interference of clouds and fog during the flight of the drone, so that the image data to be damaged. For the Anle Rice farm, the rice LAI inversion effect is not very satisfactory. There are big differences in the overall rice growth situation. The specific reasons require further field investigation and analysis.

The improved QGA-ELM algorithm based on UAV remote sensing could identify the growth level effectively and realize the effective discrimination of regional scale from the results above. Due to the group representation factors of LAI, the linear inversion models of biomass and yield were constructed at the same time which could evaluate the biomass and yield during the stage of heading and early booting, The results are shown in Table 6 that could be seen that the biomass and yield prediction model were feasible and the monomer biomass and population yield R^2P were 0.8583 and 08254, respectively, which showed better reference.

4. Discussion

(1) SVM supervised classification mapping would take occpuy lots memory resources which takes longer than ISODATA, but the classification accuracy of RGB images, MS images and HSV images presented the better classification results than ISODATA. The classification accuracy of SVM-MS in 75%, 100%, and 125% nitrogen environment was 94.46%, 97.99%, and 99.44%, respectively, from the experiment, and the overall classification accuracy was 92.14%, which showed that SVM-MS has obvious distinguishing characteristics for rice with high nitrogen content, but for ISODATA classification, there were much factors that may lead to inaccurate classification accuracy in multiple steps, compared with that SVM-MS had much existing training samples as reference; the human intervention could be also ignored, so the classification accuracy was better. So the results mentioned above proved that SVM classification could be used as the preferred classification method for nitrogen classification of rice in this paper

(2) NDVI was related to 800 nm (near-red absorption band) and 680 nm (red absorption band) from the analysis of the VI selected process in airborne multispectral band. NRI was related to red and green light absorption band around 550 nm; s_ Rep is related to the red edge near 730 nm in the near-red band; NPCI is related to the red region and the blue edge near 530 nm. R^2P and RMSE of NDVI was 0.5485, 0.7399, respectively; combined with the conclusions above, the sensitive bands which reflected rice LAI include the blue, green, and red bands. The other bands could sensitively reflect crop LAI status which confirmed the theory that LAI could not only characterize the pigment situation of crops in the unit crop planting area, but also reflected the overall situation of crop canopy

(3) The QGA-ELM was improved by using an 8-fold cross-validation combined with dynamic rotation angle strategy, single point chaotic cross operation, deterministic selection strategy, and quantum catastrophe operation that overcomes the problem of connection weight of hidden layer and threshold randomly generated in the traditional model and solves the problems of slow regression of nonlinear data and insufficient generalization ability of the model. The R^2 and RMSE of prediction set in improved QGA-ELM inversion model were 0.7396 and 0.8952, respectively; the average prediction accuracy increased by12.56%

5. Conclusion

LAI is an important physiological parameter for rice growth; traditional measurement could not realize the demand of large-scale accurate monitoring. The main purpose of this paper is to find a solution to solve the problem of regional scale accurate monitoring of rice growth through the research on the demonstration area.

(1) The aerial monitoring method based on UAV equipped with multispectral and CCD camera was adopted to get the regional scale image; compared with RGB and HSV, SVM-MS could obvious distinguish high nitrogen characteristics for rice

(2) The spectral analysis was used to realize the integration of the correlation between LAI and VI; the nonlinear relationship between NDVI, RVI, and LAI was mainly verified in this paper, and the inversion effect of ELM neural network model was better than BP and MLR model. NDVI was selected as the optimized VI; the quantitative analysis model showed a better adaptability

(3) The quantitative analysis model between LAI and NDVI was constructed to realize the accurate inversion for regional scale. QGA-ELM was innovatively proposed to solve the instability of the edge object model of the noncrop region in the linear model, combined with LS-SVR which was based on accurate classification expression solved the problems of slow regression of nonlinear data and insufficient generalization ability of the model; realize the accurate inversion and verification of different varieties LAI in four regions; clarify the universality of nonlinear expression in rice growth monitoring; and find a quantitative analysis method more suitable for rice growth remote sensing analysis

Optimizing the LAI inversion model from the perspective of improving convergence speed and applicability combined with QGA-ELM and LS-SVM in this paper, NDVI (unsaturated state) was selected as the optimal VI. Compared with others, NDVI did not need additional spectral calculation and generation which was easy to implement; technically, the validation results were intuitive and more

suitable for large-scale regional monitoring. The inversion model could accurately evaluate the growth of rice more than 5000 mu. However, there were some limitations in the research, for the data sources were based on the four main rice varieties in the 1st and 2nd accumulated temperate zones. The inversion accuracy of the 3rd, 4th, and 5th accumulated temperate zones with insufficient light still needed to be verified. The future works will focus on the effectively combining of the earlier NDVI and later RVI inversion advantages fully considering the rice varieties in the five accumulated temperate zones, hoping to form a quantitative analysis model with universality and accuracy.

Data Availability

The raw/processed data required to reproduce these findings cannot be shared at this time as the data also forms part of an ongoing study.

Conflicts of Interest

The authors declare that they have no conflicts of interest.

Acknowledgments

This work was supported by the Heilongjiang Province "Hundred Million" Engineering Science and Technology Major Special Project (NO. 2019ZX14A04), the University Nursing Program for Young Scholars with Creative Talents in Heilongjiang Province (NO. UNPYSCT-2020091), and the "YoungTalents" Project of Northeast Agricultural University (NO. 18QC22).

References

[1] K. Qiao, W. Zhu, Z. Xie, and P. Li, "Estimating the seasonal dynamics of the leaf area index using piecewise LAI-VI relationships based on phenophases," *Remote Sensing*, vol. 11, no. 6, p. 689, 2019.

[2] Z. Sha, Y. Wang, Y. Bai et al., "Comparison of leaf area index inversion for grassland vegetation through remotely sensed spectra by unmanned aerial vehicle and field-based spectroradiometer," *Journal of Plant Ecology*, vol. 12, no. 3, pp. 395–408, 2019.

[3] N. Y. Liang, G. B. Huang, P. Saratchandran, and N. Sundararajan, "Extreme learning machine: Theory and applications," *Neurocomputing*, vol. 70, no. 1-3, pp. 489–501, 2006.

[4] N. Vilfan, C. Van der Tol, O. Muller, U. Rascher, and W. Verhoef, "Fluspect-B: A model for leaf fluorescence, reflectance and transmittance spectra," *Remote Sensing of Environment*, vol. 186, no. 7, pp. 596–615, 2016.

[5] S. Jacquemoud, F. Baret, B. Andrieu, F. M. Danson, and K. Jaggard, "Extraction of vegetation biophysical parameters by inversion of the PROSPECT + SAIL models on sugar beet canopy reflectance data. Application to TM and AVIRIS sensors," *Remote Sensing of Environment*, vol. 52, no. 3, p. 35, 1995.

[6] S. K. Sinha, H. Padalia, A. Dasgupta, J. Verrelst, and J. P. Rivera, "Estimation of leaf area index using PROSAIL based LUT inversion, MLRA-GPR and empirical models: case study of tropical deciduous forest plantation, North India," *International Journal of Applied Earth Observation and Geoinformation*, vol. 86, no. 3, article 102027, 2020.

[7] Y. Zhang, J. M. Chen, J. R. Miller, and T. L. Noland, "Leaf chlorophyll content retrieval from airborne hyperspectral remote sensing imagery," *Remote Sensing of Environment*, vol. 112, no. 7, pp. 3234–3247, 2008.

[8] X. Yao, K. K. Yu, Y. J. Yang, Q. Zeng, Z. H. Chen, and J. Liu, "Estimation of Forest Leaf Area Index Based on Random Forest Model and Remote Sensing Data," *Transactions of The Chinese Society of Agricultural Machinery*, vol. 48, no. 5, pp. 159–166, 2017.

[9] L. Wang, P. Wang, S. Liang, X. Qi, L. Li, and L. Xu, "Monitoring maize growth conditions by training a BP neural network with remotely sensed vegetation temperature condition index and leaf area index," *Computers and Electronics in Agriculture*, vol. 160, no. 3, pp. 82–90, 2019.

[10] A. Capolupo, L. Kooistra, C. Berendonk, L. Boccia, and J. Suomalainen, "Estimating plant traits of grasslands from UAV-acquired hyperspectral images: a comparison of statistical approaches," *ISPRS International Journal of Geo Information*, vol. 23, no. 6, p. 14, 2019.

[11] J. Martínez, G. Egea, J. Agüera, and M. Pérez-Ruiz, "A cost-effective canopy temperature measurement system for precision agriculture: a case study on sugar beet," *Precision Agriculture*, vol. 13, no. 8, pp. 1–16, 2017.

[12] J. E. Milton, "A portable multiband radiometer for ground data collection in remote sensing," *International Journal of Remote Sensing*, vol. 1, no. 2, pp. 153–165, 1980.

[13] H. Kimm, K. Guan, C. Jiang et al., "Deriving high-spatiotemporal-resolution leaf area index for agroecosystems in the U.S. Corn Belt using Planet Labs CubeSat and STAIR fusion data," *Remote Sensing of Environment*, vol. 239, no. 3, article 111615, 2020.

[14] G. S. Krishnan and S. S. Kamath, "A novel GA-ELM model for patient-specific mortality prediction over large- scale lab event data," *Applied Soft Computing*, vol. 80, no. 5, pp. 525–533, 2019.

[15] Y. Du, P. M. Teillet, J. Cihlar, Y. Du, P. M. Teillet, and J. Cihlar, "Radiometric normalization of multitemporal high-resolution satellite images with quality control for land cover change detection," *Remote Sensing of Environment*, vol. 82, no. 1, pp. 123–134, 2002.

[16] Z. Qin, Q. Chang, B. Xie, and J. Shen, "Rice leaf nitrogen content estimation based on hysperspectral imagery of UAV in Yellow River diversion irrigation district," *Transactions of the Chinese Society of Agricultural Engineering*, vol. 32, no. 23, pp. 77–85, 2016.

[17] M. Zaman-Allah, O. Vergara, J. L. Araus et al., "Unmanned aerial platform-based multi-spectral imaging for field phenotyping of maize," *Plant Methods*, vol. 11, no. 1, p. 35, 2015.

[18] İ. Ercanlı, A. Günlü, M. Şenyurt, and S. Keleş, "Artificial neural network models predicting the leaf area index: a case study in pure even-aged Crimean pine forests from Turkey," *Forest Ecosystems*, vol. 5, no. 1, pp. 400–411, 2018.